ACS Energy LETTERS

LETTER

Visualizing Buried Local Carrier Diffusion in Halide Perovskite Crystals via Two-Photon Microscopy

Camille Stavrakas,[†,⊥] Géraud Delport,[†,⊥] Ayan A. Zhumekenov,[‡] Miguel Anaya,[†] Rosemonde Chahbazian,[†] Osman M. Bakr,[‡] Edward S. Barnard,[§] and Samuel D. Stranks*[†,‖]

[†]Cavendish Laboratory, University of Cambridge, JJ Thomson Avenue, Cambridge CB3 0HE, United Kingdom

[‡]Division of Physical Sciences and Engineering, King Abdullah University of Science and Technology (KAUST), Thuwal 23955-6900, Kingdom of Saudi Arabia

[§]Molecular Foundry, Lawrence Berkeley National Laboratory, Berkeley, California 94720, United States

[‖]Department of Chemical Engineering & Biotechnology, University of Cambridge, Philippa Fawcett Drive, Cambridge CB3 0AS, United Kingdom

Ⓢ Supporting Information

ABSTRACT: Halide perovskites have shown great potential for light emission and photovoltaic applications due to their remarkable electronic properties. Although the device performances are promising, they are still limited by microscale heterogeneities in their photophysical properties. Here, we study the impact of these heterogeneities on the diffusion of charge carriers, which are processes crucial for efficient collection of charges in light-harvesting devices. A photoluminescence tomography technique is developed in a confocal microscope using one- and two-photon excitation to distinguish between local surface and bulk diffusion of charge carriers in methylammonium lead bromide single crystals. We observe a large dispersion of local diffusion coefficients with values between 0.3 and 2 $cm^2 \cdot s^{-1}$ depending on the trap density and the morphological environment—a distribution that would be missed from analogous macroscopic or surface measurements. This work reveals a new framework to understand diffusion pathways, which are extremely sensitive to local properties and buried defects.
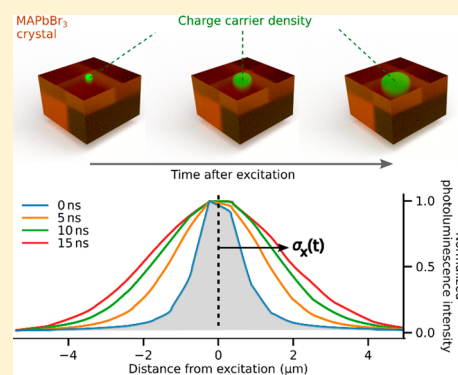
Over the past 10 years, halide perovskites have emerged as strong candidates for various light-harvesting and light-emission applications.[1−3] The performances of perovskite-based photovoltaics (PVs) and light-emitting diodes (LEDs) are now competing with mature, commercial technologies.[4] This rapid development has been made possible by the design of new halide perovskite compositions[5−7] that generally share properties of remarkably long carrier diffusion lengths ($0.1−1\ \mu m$)[8,9] even when simple cost-effective fabrication techniques are employed. However, for halide perovskites to reach their full potential, one has to understand the microscopic heterogeneities that still limit their performances.[10,11] For instance, local defects, both at the surface and inside of the bulk, trap charge carriers, thus limiting their ability to diffuse through the material. It is therefore critical to investigate the diffusion mechanisms at the local scale to identify these trap sites and elucidate ways to mitigate their influence on carrier diffusion and recombination.

Methylammonium lead bromide (MAPbBr$_3$, MA = CH$_3$NH$_3^+$) single crystals have remarkable photophysical properties, as highlighted in recent reports on amplified spontaneous emission[12] and lasing phenomena,[13,14] two-photon absorption,[15,16] extreme sensitivity to environment,[17] excitonic properties,[18,19] and long carrier diffusion lengths.[20] Additionally, their optical properties are well-documented, including their refractive index[21,22] and exciton binding energy,[23] and photon reabsorption has been quantified.[22,24,25] Such single crystals are ideal platforms to investigate intrinsic charge carrier recombination and transport because they will not be as influenced by morphological properties as their polycrystalline film counterparts, where grain boundaries may have a dominant impact on transport.[26,27] On one hand, the surface properties of these single crystals, such as defect densities[17] and carrier diffusion, have been reported.[28,29] On the other hand, optoelectronic properties are more difficult to
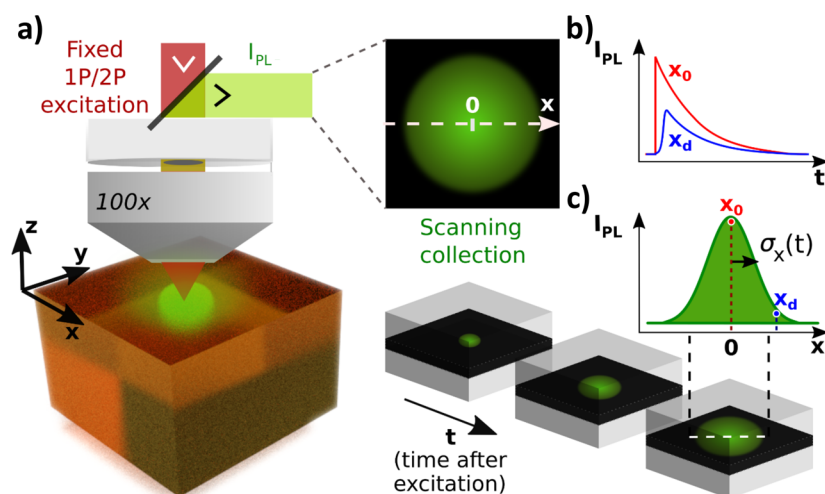
Figure 1. Overview of the time and spatially resolved PL microscope setup for measuring local carrier diffusion. (a) Schematic of the TRPL experimental setup (1P or 2P) to probe the diffusion properties laterally at different distance (x) from the excitation spot. (b) Representation of the TRPL decays that can be measured with this setup, shown here for two different x positions: x_0 (center, i.e., $x = 0$) and x_d (away from the center). (c) Artistic view of the impact of the diffusion of carriers leading to a broadening of the spatial distribution of the PL with time, including the definition of the standard deviation σ_x associated with the Gaussian distributions employed in this work.
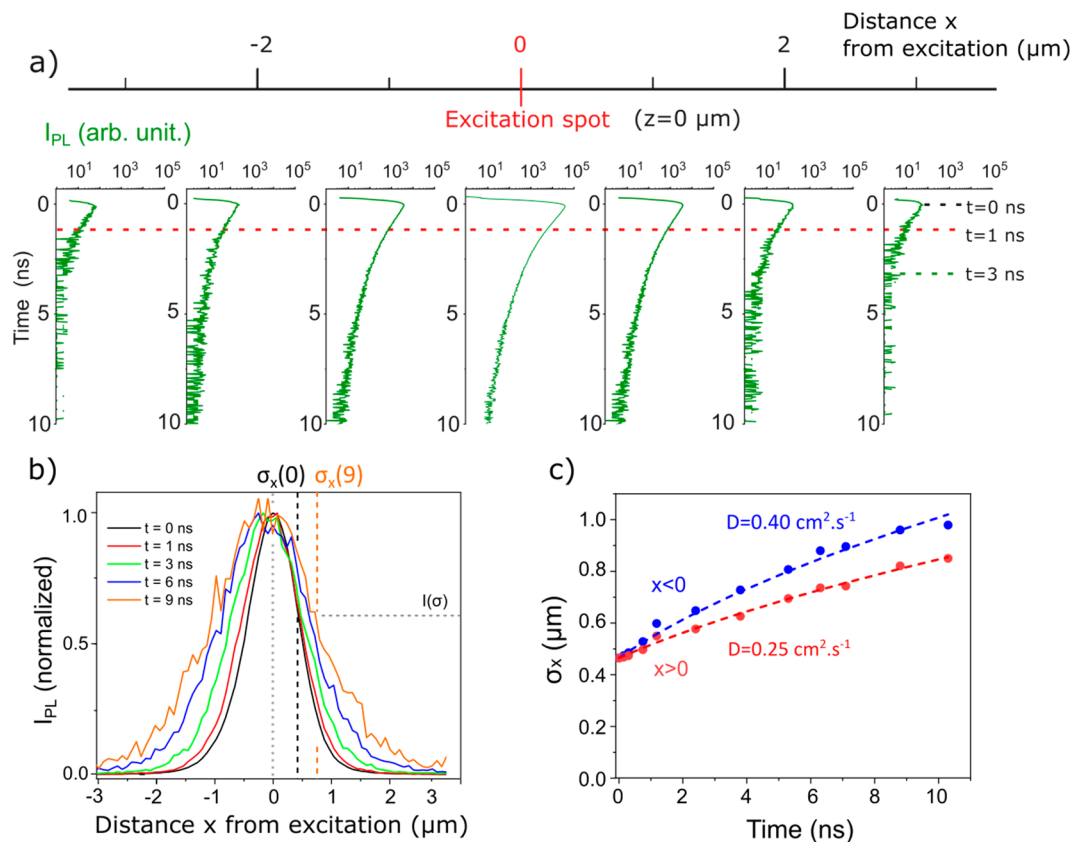
Figure 2. Surface diffusion properties in MAPbBr$_3$ single crystals. (a) TRPL decay curves at selected collection positions x with 405 nm (1P) excitation at $x = 0$, $t = 0$ (repetition rate of 10 MHz and fluence of 1.3 μJ·cm^{-2}). From these data, we extract the normalized PL intensity profiles I_{PL} as a function of time, overlaid in (b). The standard deviation $\sigma_x(t)$ extracted from Gaussian fits to the data at each time snapshot t and the corresponding PL intensity $I(\sigma)$ are also highlighted in (b). (c) Evolution of the σ_x profile broadening as a function of time extracted from the Gaussian TRPL diffusion profiles for carriers traveling to the left ($x < 0$, blue) and to the right ($x > 0$, red) of the excitation pulse. Dashed lines indicate fits to the data using eq 1 that were used to extract the diffusion coefficient values (D) stated in the panel.

probe within the bulk of these crystals, particularly on the microscale, due to the large optical absorption coefficients of these materials.[22] Time-resolved photoluminescence (TRPL) microscopy measurements allow us to study diffusive effects on

the microscale.[9,29,30] Most TRPL studies on halide perovskites to date are based on one photon (1P) excitation techniques,[8,31] which, due to the short optical absorption depth in halide perovskites,[22,24] typically probe the top ~50−
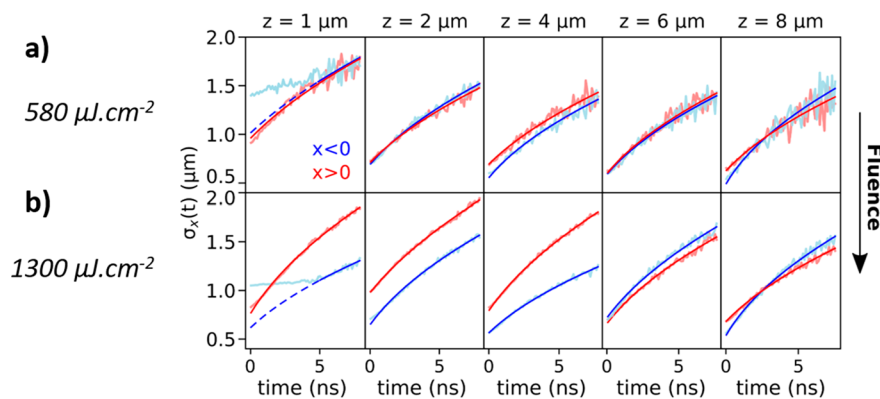
Figure 3. Bulk diffusion properties in MAPbBr$_3$ single crystals at different depths and fluences. Evolution of the σ_x profile broadening as a function of time extracted from the Gaussian TRPL diffusion profiles for $x < 0$ (blue) and $x > 0$ (red) at different depths (z) ascertained using 2P excitation (1200 nm, 8 MHz repetition rate) at a fluence of (a) 580 and (b) 1300 μJ·cm^{-2}. Solid lines are fits to the data using eq 1, with dashed lines indicating extrapolations; the extracted values are plotted in Figure 4.

100 nm of the sample with most commonly used visible excitation wavelengths. These techniques are therefore particularly sensitive to effects that are most prominent on the surface,[32−34] which include surface defects,[35] light soaking,[30] waveguiding,[36] and surface irregularities.[37] Therefore, it is not possible to observe the diffusion of charge carriers deeper in the crystal using a 1P technique. Furthermore, many studies deduce diffusion properties[8,38,39] from macroscopic 1P TRPL measurements, missing crucial local variations in carrier lifetime and diffusion properties that are ultimately responsible for power losses in devices.

Recently, we combined 1P and two-photon (2P) TRPL confocal microscopy with excitation and emission fixed at the same spatial location to unveil local, buried carrier recombination sites in halide perovskites that cannot be observed through 1P measurements alone.[40] Here, we further adapt a 1P/2P TRPL confocal microscope setup to collect the photons emitted at locations at a controllable distance away from the excitation area using a scanning collection setup.[41] By performing these diffusion measurements as a function of depth on MAPbBr$_3$ single crystals, we determine the diffusion properties in the bulk of the crystals and compare these findings with their surface diffusion properties. We use this technique to reveal a spatially and depth-dependent heterogeneous distribution of carrier diffusion properties. We then construct time and spatially resolved images of carrier diffusion and use these images to visualize buried crystal defects that have an impact on carrier transport. These results give critical insight into the factors that limit carrier transport in halide perovskite materials.

In Figure 1a, we show a general schematic of our experimental setup to probe carrier diffusion in four dimensions (time and 3D space). In general, we adjust the depth at which we generate photoexcited carriers (and probe diffusion) by using either 1P excitation ($z = 0$) or 2P excitation ($z > 0$). At a given depth, we measure a series of TRPL decay curves at different positions at distance x away from the fixed excitation spot (at $x = 0$) by raster scanning the PL collection (Figure 1b; see Supporting Information (SI) for details). In Figure 1c, we show a schematic representing the impact of the carrier diffusion on the width of the PL spatial distribution, characterized by the standard deviation σ_x of a Gaussian PL profile.

We grew MAPbBr$_3$ single crystals using an inverse temperature crystallization method[42,43] (see the SI for experimental details). We show in Figure 2a a series of example decay curves for 1P excitation ($z = 0$) in a crystal at distance x away from the local excitation spot ($x = 0$) (see Figure S3 for the full series of PL decays). We use an excitation wavelength of 405 nm and fluence of 1.3 μJ·cm^{-2}, which generates local excitation charge carrier densities on the order of $\sim 10^{17}$ cm^{-3} (see the SI for details); the PL emission peak in these samples is at $\sim$540 nm.[22,24] From these decay curves, we determine the PL intensity $I_{PL}(x,t)$ corresponding to each position x and time t after excitation. We see in Figure 2a that the I_{PL} values decrease with x as we move away from the excitation center at $x = 0$. From the TRPL curves, we can select a given time snapshot t and reconstruct the spatial profile $I_{PL}(x,t)$ of the emitted photons over the horizontal x axis (see the dotted line in Figure 2a). In Figure 2b, we show the evolution of the extracted spatial distributions in x at selected time snapshots after the initial excitation ($t = 0$) at $x = 0$ (see Figure S2 for a larger series). This spatial distribution broadens as a function of time as carriers transport away from the excitation spot.

To characterize the diffusion, we apply a Gaussian fit to the PL profiles at different time delays. This allows us to extract the standard deviation $\sigma_x(t)$ that can be interpreted as the instantaneous diffusion length at time t (see Figure 2b). In Figure 2c, we show these standard deviations as a function of time after excitation obtained from the Gaussian fits; we do this separately for the right ($x > 0$) and left ($x < 0$) sides of the excitation spot to characterize any differences in diffusion properties in each region of the crystal. The initial value of σ_x $\simeq$ 440 nm at $t = 0$ originates from a combination of factors, including the optical resolution of the setup ($\sigma_{resol} \simeq$ 180 nm in excitation at 405 nm and $\simeq$240 nm in emission at 540 nm; see the SI for details) and the possibility of early time diffusion or reabsorbed photons emitted at early times[44] within the temporal instrument response of the setup ($\simeq$100 ps).

In a classical diffusive scenario, the quantity $\sigma_x(t)$ follows the form[41]

$$\sigma_x^2(t) = \sigma_x^2(0) + 2Dt \tag{1}$$

where D is the carrier diffusion coefficient (see SI for derivation). We find that the evolution of σ is well-fitted by this linear expression in both regions (dashed lines in Figure

2c). From these fits, we obtain a diffusion coefficient of $D = 0.40$ cm$^2 \cdot$s^{-1} for the $x < 0$ region and $D = 0.25$ cm$^2 \cdot$s^{-1} for the $x > 0$ region. These two values are significantly different, showing that charge carriers diffuse more efficiently on one side than on the other, in line with local heterogeneity in optoelectronic properties in halide perovskites.[11,40] This spatial asymmetry in the diffusion coefficient is also seen in the PL profiles in Figure 2b, which becomes increasingly asymmetric about $x = 0$ with time. The measured diffusion coefficients are lower but of the same order of magnitude to previously reported values on similar crystals ($\simeq 1$ cm$^2 \cdot$s^{-1}[45]). We observe a higher diffusion coefficient of $D = 0.57$ cm$^2 \cdot$s^{-1} on another region of the same crystal (see Figure S2), further highlighting the spatial variation of the diffusion properties and the need for microscopic techniques to visualize such variations. We note that here we are not considering other carrier recombination processes that will also act to change the background local carrier density, but the good fits of the extracted data to eq 1 suggest that diffusive processes dominate for the samples and excitation conditions used in this work.

After elucidating the local surface diffusion properties ($z = 0$) using 1P excitation, we now seek to understand the diffusion properties in the bulk of a MAPbBr$_3$ crystal by selectively exciting at a particular depth ($z > 0$) using 2P excitation (1200 nm wavelength). For this purpose, we have used 2P excitation to probe a different area of a MAPbBr$_3$ crystal at selected depth ($z > 0$). In this configuration, our excitation depth resolution is $\simeq 1.5$ μm, and our lateral resolution is $\sigma_{laser} \simeq 0.5$ μm (see the SI for details). We note that we use a long-pass filter to extract only the low-energy tail of the emitted photons to minimize reabsorption effects that could attenuate the higher-energy photons. We show 2P diffusion profiles as a function of depth z in Figure 3a with a 2P fluence of 580 μJ$\cdot$cm^{-2}, which generates a comparable charge excitation density in the samples to the 1P measurements (i.e., $\sim 10^{17}$ cm^{-3}; see the SI for details). For each depth, we once again separately treat the regions to the left ($x < 0$) and the right ($x > 0$). Near the surface at $z = 1$ μm, we observe a relatively broad initial PL distribution, $\sigma_x(0)$, for the left ($x < 0$) region, which stays constant over several nanoseconds, before showing the classical diffusion dependence of eq 1 at later times. We attribute this observation over the first few nanoseconds to be a result of a light-soaking (photodarkening) effect on the surface due to the extended time required for the 2P measurements, with the local extent of this effect depending on the local PL heterogeneity and local carrier density;[30,46] we note that we also observe this effect in 1P excitation when illuminating for extended times (Figure S4). By contrast, the temporal evolution of $\sigma_x(t)$ when probing deeper into the crystal, where light-soaking effects are far less apparent,[40] fits well to the classical diffusion square root law (eq 1) across all times (see also Figure S9), and we obtain similar diffusion properties in both the left ($x < 0$) and right ($x > 0$) regions. We note that the same measurements performed on different regions and on crystals with different compositions (e.g., MAPbI$_3$) reveal different behavior, suggesting that we are indeed probing the local behavior in the specific region of interest without experimental artifacts (see Figure S10). We show the depth-dependent diffusion coefficients in Figure 4a, revealing relatively homogeneous values ranging between 0.9 and 1.6 cm$^2 \cdot$s^{-1} for $x < 0$ and $x > 0$ (see statistical distributions in Figure 4c at all depths and regions). These values are notably higher than the values obtained at the surface ($\simeq 0.3$
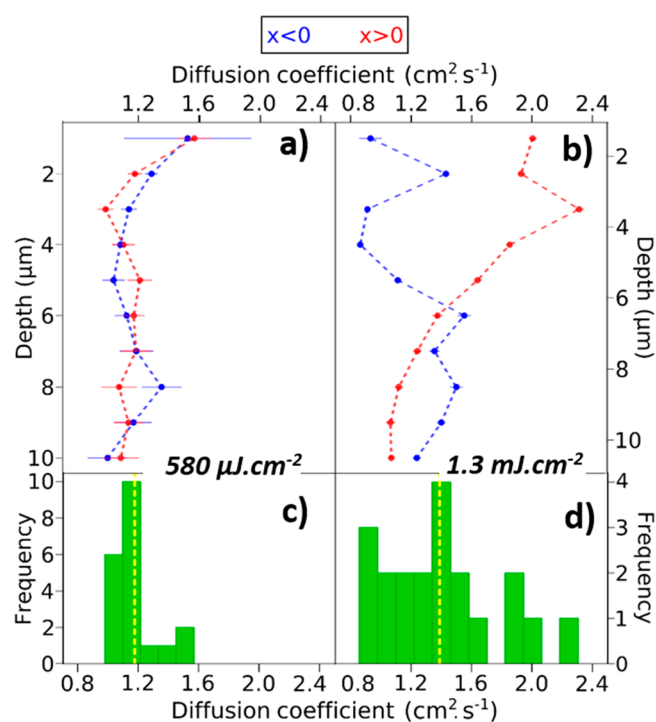
Figure 4. Statistics of the depth-dependent diffusion coefficients in MAPbBr$_3$ single crystals. The depth-dependent (z) diffusion coefficients (D) obtained from fits to the diffusion plots in Figure 3 using eq 1, with excitation fluence of (a) 580 and (b) 1300 μJ$\cdot$cm^{-2}. The regions $x < 0$ (blue) and $x > 0$ (red) are shown. The corresponding histograms of diffusion coefficients across all depths (z) and directions (x) are shown for the excitation fluences of (c) 580 and (d) 1300 μJ$\cdot$cm^{-2}. The diffusion coefficients for the same z values are here binned together independently of the direction of carriers ($x < 0$ or $x > 0$). The dashed yellow lines denote the mean values of the distributions, which are $\simeq 1.2$ and $\simeq 1.4$ cm$^2 \cdot$s^{-1}, respectively.

cm$^2 \cdot$s^{-1}) and match the highest diffusion coefficients reported from 1P TRPL measurements on MAPbBr$_3$ crystals.[29] The larger values of the diffusion coefficient in the bulk than the surface are consistent with the majority of traps residing at the surface, which may limit carrier diffusion in that region.[47,48]

To investigate these observations further, we show in Figure 3b the temporal evolution of $\sigma_x(t)$ with higher photoexcitation density (1300 μJ$\cdot$cm^{-2}) and the corresponding extracted depth-dependent diffusion coefficients in Figure 4b. We see a striking increase in the diffusion coefficients at a range of depths particularly for the left ($x < 0$) region when compared to the lower fluence measurements. For some depth profiles, the values now reach 2 cm$^2 \cdot$s^{-1}, thus even exceeding previously reported values.[29] Along with the global increase, we observe a wider distribution of diffusion coefficient values (see Figure 4d). We note that as the fluence increases and the diffusion coefficients generally increase, the measured PL decay times globally decrease from around $\simeq 6$ ns to less than 4 ns (see Figure S6) for most of the PL profiles. We attribute these combined observations to a larger saturation of traps at higher fluences,[40,49,50] leading to more efficient diffusion of charge carriers and increased bimolecular recombination (as seen from the shorter PL lifetimes at higher fluence[49]). We note, however, that this saturation of traps is not uniform across all regions, with the diffusion coefficients at some depths remaining relatively unchanged at $\simeq 1$ cm$^2 \cdot$s^{-1} at higher
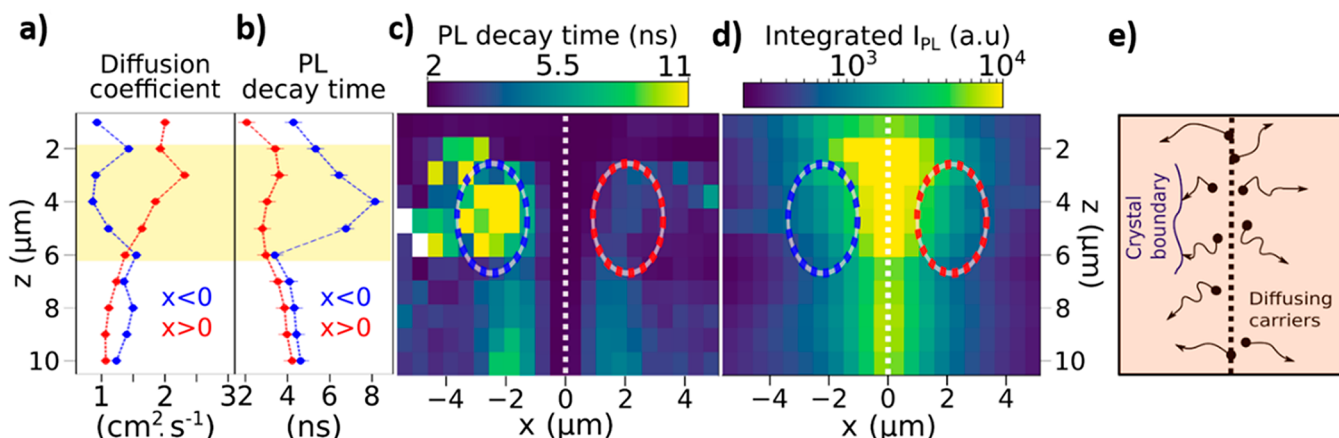
Figure 5. Visualizing a crystal boundary through photophysical measurements. (a) Diffusion coefficient and (b) PL decay times (defined as the time taken to fall to $1/e$ of the initial intensity; see the SI), averaged over the lateral profiles in each region at each depth as a function of depth, as extracted from the data in Figure 3. The regions $x < 0$ and $x > 0$ are denoted blue and red, respectively, and a region of interest is highlighted by yellow shading. x−z slices of the (c) PL decay time and (d) integrated PL intensity of the same region as those in (a) and (b). Regions of interest discussed in the text are highlighted with blue ($x < 0$) and red ($x > 0$) dashed circles. (e) Schematic showing the impact of a buried crystal boundary on the diffusion of carriers initially excited at $x = 0$ (dashed line).

fluence. This observation suggests that there are heterogeneous distributions of trap densities and perhaps even variations in types of traps below the surface. These local variations in diffusion coefficient laterally and with depth would be missed using macroscopic measurements, which would provide only the average diffusion values denoted by the distributions ($\simeq 1.2$ and $\simeq 1.4$ cm$^2 \cdot$s^{-1}, as shown by a yellow dashed line in Figure 4c,d, respectively). These variations would also be missed using 1P PL measurements alone, which would probe only the surface. Therefore, these local, depth-dependent results demonstrate the unique insight obtained by using the 2P microscopic technique.

To better understand these heterogeneities, we display side-by-side in Figure 5 several important photophysical parameters obtained from the higher-fluence (1300 μJ·cm^{-2}) 2P measurements for a range of spatial (x) and depth (z) values (see Figure S11 for plots of other parameters). The diffusion behavior is highly asymmetric even below the surface as large differences can be observed between the $x > 0$ and $x < 0$ profiles (Figure 5a). This is particularly evident between $z = 2$ and 6 μm (see the yellow shaded area in Figure 5a,b), where we now focus our analysis. We observe that the diffusion coefficients are much larger for $x > 0$ ($\simeq 2$ cm$^2 \cdot$s^{-1}) than those for $x < 0$ ($\simeq 1$ cm$^2 \cdot$s^{-1}). In Figure 5b, we show the PL decay time (defined as the time taken for the PL to fall to $1/e$ of its initial intensity; see the SI), averaged over the $x < 0$ or $x > 0$ lateral profile at each depth. We find that the PL decay time follows a very different trend than that of the diffusion coefficients as the larger decay times are found on the $x < 0$ side ($\simeq 4$−8 ns) while the decay times for $x > 0$ are appreciably shorter ($\simeq 2$−4 ns). In fact, the diffusion coefficients and PL decay times are anticorrelated in these two particular regions of the crystal. In Figure 5c, we show an x−z image of the PL decay times (measured after excitation at $x = 0$ for each depth). We see that the longer decay times for the $x < 0$ region are measured over a region of several microns (inside the blue dashed circled region), extending in both x and z directions in that region. On the other side of the excitation region ($x > 0$, red dashed circle), the decay times are comparatively lower and more spatially homogeneous. Additionally, the integrated PL intensity in the $x < 0$ region (blue dashed circle) is a factor

of 1.7 lower than that in the $x > 0$ region (Figure 5d; see Figure S12).

Given that there is a long PL lifetime but short diffusion coefficient and lower PL counts in the $x < 0$ region, we propose the presence of a defective crystal boundary between domains (Figure 5e) in the region in the blue dashed circle in Figure 5c,d. Indeed, edges and boundaries in halide perovskite crystals have been previously proposed to inhibit the diffusion of charge carriers.[9] Therefore, charge carriers moving through this $x < 0$ area would be impeded from moving further beyond this boundary, leading to a lower effective diffusion coefficient in the region (see Figure 5e). Additionally, this model also explains why the increase in local carrier excitation density (fluence) has a negligible influence on the diffusion properties in this $x < 0$ region; such a physical barrier preventing the transport of charges may correspond to a defect type that is not able to be saturated in the same way as other point or extended defects, such as those in the $x > 0$ region. Indeed, boundaries often present a larger concentration of nonradiative recombination sites in halide perovskite materials,[11,51] and their increased influence in that region may also explain the extended PL lifetime albeit lower PL intensity in that local region; such a combination is a signature of a trap-limited regime in which there is a lower fraction of radiative bimolecular recombination relative to nonradiative monomolecular processes that can have apparently longer lifetimes.[49] Therefore, we conclude that charges near this boundary are significantly trapped, while the carriers at other depths are more freely able to diffuse (see Figure 5e).

In conclusion, we have developed a microscope platform to visualize in four dimensions (time and 3D space) carrier diffusion in different regions and depths of a semiconducting sample. We demonstrate its application on MAPbBr$_3$ single crystals, revealing local variations in charge carrier diffusion on the microscale. At the surface, the diffusion is hindered by charge carrier traps but deeper in the sample we observe much larger diffusion coefficients that can even locally exceed the highest values reported in the literature from 1P TRPL measurements ($\simeq 1$ cm$^2 \cdot$s^{-1}[29]). We use this technique to reveal a region in which carrier diffusion is impeded even deeper into the crystal, which we interpret as a buried crystal boundary.

This study demonstrates the capabilities of 2P TRPL tomography to visualize buried heterogeneities that would remain undetected with conventional 1P microscopy or macroscopic approaches. We expect that the technique will be useful for a variety of semiconducting systems, ultimately providing guidance to improve the optoelectronic performance of devices.

■ ASSOCIATED CONTENT

Ⓢ Supporting Information

The Supporting Information is available free of charge at https://pubs.acs.org/doi/10.1021/acsenergylett.9b02244.

Experimental section, including the synthesis of the perovskites crystal, details of the one-photon and two-photon experimental setups, additional time-resolved PL, and diffusion data, and details about the diffusion model and simulation (PDF)

■ AUTHOR INFORMATION

Corresponding Author

*E-mail: sds65@cam.ac.uk.

ORCID Ⓞ

Ayan A. Zhumekenov: 0000-0002-3216-5315
Miguel Anaya: 0000-0002-0384-5338
Osman M. Bakr: 0000-0002-3428-1002
Samuel D. Stranks: 0000-0002-8303-7292

Author Contributions

⊥C.S. and G.D. contributed equally to this work.

Notes

The authors declare no competing financial interest.

■ ACKNOWLEDGMENTS

■ REFERENCES

(1) Liu, M.; Johnston, M. B.; Snaith, H. J. Efficient Planar Heterojunction Perovskite Solar Cells by Vapour Deposition. *Nature* **2013**, *501* (7467), 395.

(2) Luo, J.; Im, J.-H.; Mayer, M. T.; Schreier, M.; Nazeeruddin, M. K.; Park, N.-G.; Tilley, S. D.; Fan, H. J.; Grätzel, M. Water Photolysis at 12.3% Efficiency via Perovskite Photovoltaics and Earth-Abundant Catalysts. *Science* **2014**, *345* (6204), 1593−1596.

(3) Yuan, M.; Quan, L. N.; Comin, R.; Walters, G.; Sabatini, R.; Voznyy, O.; Hoogland, S.; Zhao, Y.; Beauregard, E. M.; Kanjanaboos, P.; et al. Perovskite Energy Funnels for Efficient Light-Emitting Diodes. *Nat. Nanotechnol.* **2016**, *11* (10), 872.

(4) *NREL Efficiency Chart*. https://www.nrel.gov/pv/assets/pdfs/best-research-cell-efficiencies.20191106.pdf (2019).

(5) Saliba, M.; Matsui, T.; Seo, J.-Y.; Domanski, K.; Correa-Baena, J.-P.; Nazeeruddin, M. K.; Zakeeruddin, S. M.; Tress, W.; Abate, A.; Hagfeldt, A.; et al. Cesium-Containing Triple Cation Perovskite Solar Cells: Improved Stability, Reproducibility and High Efficiency. *Energy Environ. Sci.* **2016**, *9* (6), 1989−1997.

(6) Tsai, H.; Nie, W.; Blancon, J.-C.; Stoumpos, C. C.; Asadpour, R.; Harutyunyan, B.; Neukirch, A. J.; Verduzco, R.; Crochet, J. J.; Tretiak, S.; et al. High-Efficiency Two-Dimensional Ruddlesden−Popper Perovskite Solar Cells. *Nature* **2016**, *536* (7616), 312.

(7) Noel, N. K.; Stranks, S. D.; Abate, A.; Wehrenfennig, C.; Guarnera, S.; Haghighirad, A.-A.; Sadhanala, A.; Eperon, G. E.; Pathak, S. K.; Johnston, M. B.; et al. Lead-Free Organic−Inorganic Tin Halide Perovskites for Photovoltaic Applications. *Energy Environ. Sci.* **2014**, *7* (9), 3061−3068.

(8) Stranks, S. D.; Eperon, G. E.; Grancini, G.; Menelaou, C.; Alcocer, M. J. P.; Leijtens, T.; Herz, L. M.; Petrozza, A.; Snaith, H. J. Electron-Hole Diffusion Lengths Exceeding 1 Micrometer in an Organometal Trihalide Perovskite Absorber. *Science* **2013**, *342* (6156), 341−344.

(9) Ciesielski, R.; Schäfer, F.; Hartmann, N. F.; Giesbrecht, N.; Bein, T.; Docampo, P.; Hartschuh, A. Grain Boundaries Act as Solid Walls for Charge Carrier Diffusion in Large Crystal MAPI Thin Films. *ACS Appl. Mater. Interfaces* **2018**, *10* (9), 7974−7981.

(10) Tennyson, E. M.; Doherty, T. A. S.; Stranks, S. D. Heterogeneity at Multiple Length Scales in Halide Perovskite Semiconductors. *Nat. Rev. Mater.* **2019**, *4*, 573.

(11) de Quilettes, D. W.; Vorpahl, S. M.; Stranks, S. D.; Nagaoka, H.; Eperon, G. E.; Ziffer, M. E.; Snaith, H. J.; Ginger, D. S. Impact of Microstructure on Local Carrier Lifetime in Perovskite Solar Cells. *Science* **2015**, *348* (6235), 683−686.

(12) Priante, D.; Dursun, I.; Alias, M. S.; Shi, D.; Melnikov, V. A.; Ng, T. K.; Mohammed, O. F.; Bakr, O. M.; Ooi, B. S. The Recombination Mechanisms Leading to Amplified Spontaneous Emission at the True-Green Wavelength in CH3NH3PbBr3 Perovskites. *Appl. Phys. Lett.* **2015**, *106* (8), 081902.

(13) Gu, Z.; Wang, K.; Sun, W.; Li, J.; Liu, S.; Song, Q.; Xiao, S. Two-photon Pumped CH3NH3PbBr3 Perovskite Microwire Lasers. *Adv. Opt. Mater.* **2016**, *4* (3), 472−479.

(14) Zhu, H.; Fu, Y.; Meng, F.; Wu, X.; Gong, Z.; Ding, Q.; Gustafsson, M. V.; Trinh, M. T.; Jin, S.; Zhu, X. Y. Lead Halide Perovskite Nanowire Lasers with Low Lasing Thresholds and High Quality Factors. *Nat. Mater.* **2015**, *14* (6), 636.

(15) Walters, G.; Sutherland, B. R.; Hoogland, S.; Shi, D.; Comin, R.; Sellan, D. P.; Bakr, O. M.; Sargent, E. H. Two-Photon Absorption in Organometallic Bromide Perovskites. *ACS Nano* **2015**, *9* (9), 9340−9346.

(16) Zhang, W.; Peng, L.; Liu, J.; Tang, A.; Hu, J.; Yao, J.; Zhao, Y. S. Controlling the Cavity Structures of Two-Photon-Pumped Perovskite Microlasers. *Adv. Mater.* **2016**, *28* (21), 4040−4046.

(17) Fang, H.-H.; Adjokatse, S.; Wei, H.; Yang, J.; Blake, G. R.; Huang, J.; Even, J.; Loi, M. A. Ultrahigh Sensitivity of Methylammonium Lead Tribromide Perovskite Single Crystals to Environmental Gases. *Sci. Adv.* **2016**, *2* (7), e1600534.

(18) Tilchin, J.; Dirin, D. N.; Maikov, G. I.; Sashchiuk, A.; Kovalenko, M. V.; Lifshitz, E. Hydrogen-like Wannier−Mott Excitons in Single Crystal of Methylammonium Lead Bromide Perovskite. *ACS Nano* **2016**, *10* (6), 6363−6371.

(19) Bouteyre, P.; Nguyen, H. S.; Lauret, J.-S.; Trippé-Allard, G.; Delport, G.; Lédée, F.; Diab, H.; Belarouci, A.; Seassal, C.; Garrot, D.; et al. Room-Temperature Cavity Polaritons with 3D Hybrid Perovskite: Toward Large-Surface Polaritonic Devices. *ACS Photonics* **2019**, *6* (7), 1804−1811.

(20) Shi, D.; Adinolfi, V.; Comin, R.; Yuan, M.; Alarousu, E.; Buin, A.; Chen, Y.; Hoogland, S.; Rothenberger, A.; Katsiev, K.; et al. Low Trap-State Density and Long Carrier Diffusion in Organolead

Trihalide Perovskite Single Crystals. *Science* **2015**, *347* (6221), 519−522.

(21) Brittman, S.; Garnett, E. C. Measuring n and k at the Microscale in Single Crystals of CH3NH3PbBr3 Perovskite. *J. Phys. Chem. C* **2016**, *120* (1), 616−620.

(22) Wenger, B.; Nayak, P. K.; Wen, X.; Kesava, S. V.; Noel, N. K.; Snaith, H. J. Consolidation of the Optoelectronic Properties of CH3NH3PbBr3 Perovskite Single Crystals. *Nat. Commun.* **2017**, *8* (1), 590.

(23) Galkowski, K.; Mitioglu, A.; Miyata, A.; Plochocka, P.; Portugall, O.; Eperon, G. E.; Wang, J. T.-W.; Stergiopoulos, T.; Stranks, S. D.; Snaith, H. J.; et al. Determination of the Exciton Binding Energy and Effective Masses for Methylammonium and Formamidinium Lead Tri-Halide Perovskite Semiconductors. *Energy Environ. Sci.* **2016**, *9* (3), 962−970.

(24) Diab, H.; Arnold, C.; Lédée, F.; Trippé-Allard, G.; Delport, G.; Vilar, C.; Bretenaker, F.; Barjon, J.; Lauret, J.-S.; Deleporte, E.; et al. Impact of Reabsorption on the Emission Spectra and Recombination Dynamics of Hybrid Perovskite Single Crystals. *J. Phys. Chem. Lett.* **2017**, *8* (13), 2977−2983.

(25) Yamada, T.; Yamada, Y.; Nakaike, Y.; Wakamiya, A.; Kanemitsu, Y. Photon Emission and Reabsorption Processes in CH$_3$NH$_3$PbBr$_3$ Single Crystals Revealed by Time-Resolved Two-Photon-Excitation Photoluminescence Microscopy. *Phys. Rev. Appl.* **2017**, *7* (1), 14001.

(26) Nie, W.; Tsai, H.; Asadpour, R.; Blancon, J.-C.; Neukirch, A. J.; Gupta, G.; Crochet, J. J.; Chhowalla, M.; Tretiak, S.; Alam, M. A.; et al. High-Efficiency Solution-Processed Perovskite Solar Cells with Millimeter-Scale Grains. *Science (Washington, DC, U. S.)* **2015**, *347* (6221), 522−525.

(27) Chu, Z.; Yang, M.; Schulz, P.; Wu, D.; Ma, X.; Seifert, E.; Sun, L.; Li, X.; Zhu, K.; Lai, K. Impact of Grain Boundaries on Efficiency and Stability of Organic-Inorganic Trihalide Perovskites. *Nat. Commun.* **2017**, *8* (1), 2230.

(28) Handloser, K.; Giesbrecht, N.; Bein, T.; Docampo, P.; Handloser, M.; Hartschuh, A. Contactless Visualization of Fast Charge Carrier Diffusion in Hybrid Halide Perovskite Thin Films. *ACS Photonics* **2016**, *3* (2), 255−261.

(29) Tian, W.; Zhao, C.; Leng, J.; Cui, R.; Jin, S. Visualizing Carrier Diffusion in Individual Single-Crystal Organolead Halide Perovskite Nanowires and Nanoplates. *J. Am. Chem. Soc.* **2015**, *137* (39), 12458−12461.

(30) DeQuilettes, D. W.; Zhang, W.; Burlakov, V. M.; Graham, D. J.; Leijtens, T.; Osherov, A.; Bulović, V.; Snaith, H. J.; Ginger, D. S.; Stranks, S. D. Photo-Induced Halide Redistribution in Organic−Inorganic Perovskite Films. *Nat. Commun.* **2016**, *7*, 11683.

(31) Bercegol, A.; Ramos, F. J.; Rebai, A.; Guillemot, T.; Ory, D.; Rousset, J.; Lombez, L. Slow Diffusion and Long Lifetime in Metal Halide Perovskites for Photovoltaics. *J. Phys. Chem. C* **2018**, *122* (43), 24570−24577.

(32) Stewart, R. J.; Grieco, C.; Larsen, A. V.; Maier, J. J.; Asbury, J. B. Approaching Bulk Carrier Dynamics in Organo-Halide Perovskite Nanocrystalline Films by Surface Passivation. *J. Phys. Chem. Lett.* **2016**, *7* (7), 1148−1153.

(33) Murali, B.; Dey, S.; Abdelhady, A. L.; Peng, W.; Alarousu, E.; Kirmani, A. R.; Cho, N.; Sarmah, S. P.; Parida, M. R.; Saidaminov, M. I.; et al. Surface Restructuring of Hybrid Perovskite Crystals. *ACS Energy Lett.* **2016**, *1* (6), 1119−1126.

(34) Sarmah, S. P.; Burlakov, V. M.; Yengel, E.; Murali, B.; Alarousu, E.; El-Zohry, A. M.; Yang, C.; Alias, M. S.; Zhumekenov, A. A.; Saidaminov, M. I.; et al. Double Charged Surface Layers in Lead Halide Perovskite Crystals. *Nano Lett.* **2017**, *17* (3), 2021−2027.

(35) Correa-Baena, J.-P.; Turren-Cruz, S.-H.; Tress, W.; Hagfeldt, A.; Aranda, C.; Shooshtari, L.; Bisquert, J.; Guerrero, A. Changes from Bulk to Surface Recombination Mechanisms between Pristine and Cycled Perovskite Solar Cells. *ACS Energy Lett.* **2017**, *2* (3), 681−688.

(36) Dursun, I.; Zheng, Y.; Guo, T.; De Bastiani, M.; Turedi, B.; Sinatra, L.; Haque, M. A.; Sun, B.; Zhumekenov, A. A.; Saidaminov, M. I.; et al. Efficient Photon Recycling and Radiation Trapping in Cesium Lead Halide Perovskite Waveguides. *ACS Energy Lett.* **2018**, *3* (7), 1492−1498.

(37) Tachikawa, T.; Karimata, I.; Kobori, Y. Surface Charge Trapping in Organolead Halide Perovskites Explored by Single-Particle Photoluminescence Imaging. *J. Phys. Chem. Lett.* **2015**, *6* (16), 3195−3201.

(38) Herz, L. M. Charge-Carrier Mobilities in Metal Halide Perovskites: Fundamental Mechanisms and Limits. *ACS Energy Lett.* **2017**, *2* (7), 1539−1548.

(39) Ning, W.; Wang, F.; Wu, B.; Lu, J.; Yan, Z.; Liu, X.; Tao, Y.; Liu, J.; Huang, W.; Fahlman, M.; et al. Long Electron−Hole Diffusion Length in High-Quality Lead-Free Double Perovskite Films. *Adv. Mater.* **2018**, *30* (20), 1706246.

(40) Stavrakas, C.; Zhumekenov, A. A.; Brenes, R.; Abdi-Jalebi, M.; Bulović, V.; Bakr, O. M.; Barnard, E. S.; Stranks, S. D. Probing Buried Recombination Pathways in Perovskite Structures Using 3D Photoluminescence Tomography. *Energy Environ. Sci.* **2018**, *11* (10), 2846−2852.

(41) Akselrod, G. M.; Prins, F.; Poulikakos, L. V.; Lee, E. M. Y.; Weidman, M. C.; Mork, A. J.; Willard, A. P.; Bulović, V.; Tisdale, W. A. Subdiffusive Exciton Transport in Quantum Dot Solids. *Nano Lett.* **2014**, *14* (6), 3556−3562.

(42) Saidaminov, M. I.; Abdelhady, A. L.; Maculan, G.; Bakr, O. M. Retrograde Solubility of Formamidinium and Methylammonium Lead Halide Perovskites Enabling Rapid Single Crystal Growth. *Chem. Commun.* **2015**, *51* (100), 17658−17661.

(43) Saidaminov, M. I.; Abdelhady, A. L.; Murali, B.; Alarousu, E.; Burlakov, V. M.; Peng, W.; Dursun, I.; Wang, L.; He, Y.; Maculan, G.; et al. High-Quality Bulk Hybrid Perovskite Single Crystals within Minutes by Inverse Temperature Crystallization. *Nat. Commun.* **2015**, *6*, 7586.

(44) Richter, J. M.; Chen, K.; Sadhanala, A.; Butkus, J.; Rivett, J. P. H.; Friend, R. H.; Monserrat, B.; Hodgkiss, J. M.; Deschler, F. Direct Bandgap Behavior in Rashba-Type Metal Halide Perovskites. *Adv. Mater.* **2018**, *30* (52), 1803379.

(45) Sridharan, A.; Noel, N. K.; Hwang, H.; Hafezian, S.; Rand, B. P.; Kéna-Cohen, S. Time-Resolved Imaging of Non-Diffusive Carrier Transport in Long-Lifetime Halide Perovskite Thin Films. *arXiv Prepr. arXiv1905.11242* **2019**.

(46) Brenes, R.; Eames, C.; Bulović, V.; Islam, M. S.; Stranks, S. D. The Impact of Atmosphere on the Local Luminescence Properties of Metal Halide Perovskite Grains. *Adv. Mater.* **2018**, *30* (15), 1706208.

(47) Gong, X.; Huang, Z.; Sabatini, R.; Tan, C.-S.; Bappi, G.; Walters, G.; Proppe, A.; Saidaminov, M. I.; Voznyy, O.; Kelley, S. O.; et al. Contactless Measurements of Photocarrier Transport Properties in Perovskite Single Crystals. *Nat. Commun.* **2019**, *10* (1), 1591.

(48) deQuilettes, D. W.; Jariwala, S.; Burke, S.; Ziffer, M. E.; Wang, J. T.-W.; Snaith, H. J.; Ginger, D. S. Tracking Photoexcited Carriers in Hybrid Perovskite Semiconductors: Trap-Dominated Spatial Heterogeneity and Diffusion. *ACS Nano* **2017**, *11* (11), 11488−11496.

(49) Stranks, S. D.; Burlakov, V. M.; Leijtens, T.; Ball, J. M.; Goriely, A.; Snaith, H. J. Recombination Kinetics in Organic-Inorganic Perovskites: Excitons, Free Charge, and Subgap States. *Phys. Rev. Appl.* **2014**, *2* (3), 34007.

(50) Yang, Y.; Yang, M.; Li, Z.; Crisp, R.; Zhu, K.; Beard, M. C. Comparison of Recombination Dynamics in CH3NH3PbBr3 and CH3NH3PbI3 Perovskite Films: Influence of Exciton Binding Energy. *J. Phys. Chem. Lett.* **2015**, *6* (23), 4688−4692.

(51) Park, J.-S.; Calbo, J.; Jung, Y.-K.; Whalley, L. D.; Walsh, A. Accumulation of Deep Traps at Grain Boundaries in Halide Perovskites. *ACS Energy Lett.* **2019**, *4*, 1321−1327.